Target polarization for $^2\vec{\mathrm{H}}(e,e'p)n$ at GeV energies

Sabine Jeschonnek[1] and J. W. Van Orden[2,3]
[1]*The Ohio State University, Physics Department, Lima, Ohio 45804, USA*
[2]*Department of Physics, Old Dominion University, Norfolk, Virginia 23529, USA*
[3]*Thomas Jefferson National Accelerator Facility, 12000 Jefferson Ave., Newport News, Virginia 23606, USA*
(Received 22 July 2009; published 9 November 2009)

We perform a fully relativistic calculation of the $^2\vec{\mathrm{H}}(e,e'p)n$ reaction in the impulse approximation employing the Gross equation to describe the deuteron ground state, and we use the SAID parametrization of the full NN scattering amplitude to describe the final state interactions (FSIs). The formalism for treating target polarization with arbitrary polarization axes is discussed, and general properties of some asymmetries are derived from it. We show results for momentum distributions and angular distributions of various asymmetries that can only be accessed with polarized targets.

DOI: 10.1103/PhysRevC.80.054001 PACS number(s): 25.30.Fj, 21.45.Bc, 24.10.Jv

I. INTRODUCTION

There are many interesting questions to be answered in investigating exclusive electron scattering from the deuteron: What does the nuclear ground state look like at short distances? Are there any six-quark contributions to the wave function? When does a description in terms of hadronic degrees of freedom break down? To answer any of these questions, a precise understanding of the reaction mechanism is mandatory. Final state interactions are the most relevant components of the reaction mechanism at GeV energies, but meson exchange currents and isobar states will also contribute. The fact that the deuteron is the simplest nucleus enables us to study all facets of the reaction mechanism in great detail. Anything that can be gleaned from the deuteron will be highly useful for heavier nuclei. Exclusive electron scattering from nuclei is one type of reaction in which one may observe color transparency [1], and the deuteron itself provides a laboratory for the study of neutrons, e.g., the neutron magnetic form factor [2]. The short-range structures studied in exclusive electron scattering might even reveal information about the properties of neutron stars [3]. For some recent reviews of exclusive electron scattering, see, e.g., Refs. [4–6].

Recently [7], we performed a fully relativistic calculation of the $^2\mathrm{H}(e,e'p)n$ reaction, using a relativistic wave function [8] and NN scattering data [9] for our calculation of the full, spin-dependent final state interactions (FSIs). The main difference from many other high quality calculations using the generalized eikonal approximation [10–12] or a diagrammatic approach [13] is the inclusion of all the spin-dependent pieces in the nucleon-nucleon amplitude. Full FSIs have recently been included in Ref. [14]. Several experiments with unpolarized deuterons are currently under analysis or have been published recently, [2,15–18]. There are also new proposals for $^2\mathrm{H}(e,e'p)$ experiments at the Thomas Jefferson National Accelerator Facility (Jefferson Lab) [19].

In Ref. [7], we focused on observables that are accessible for an unpolarized target and an unpolarized nucleon detected in the final state. The spin-dependent pieces in our FSI calculation were particularly relevant for the fifth response function, an observable that can be measured only with polarized electron beams. Naturally, experiments with polarization of the target or ejectile are harder to perform than their unpolarized counterparts. However, the extra effort allows one to study otherwise inaccessible observables that are rather sensitive to certain properties of the nuclear ground state and the reaction mechanism. In this paper, we investigate the asymmetries that can be measured with a polarized deuteron target. These observables are of particular interest to us because we have a precise, fully spin-dependent description of the final state interactions. As before, the focus of our numerical calculations is the kinematic region accessible at GeV energies, i.e., the kinematic range of Jefferson Lab. Currently, some deuteron target polarization data taken in Jefferson Lab's Hall B are being analyzed [20]. At lower energies, measurements of the beam-vector asymmetry A_{ed}^V have been performed at NIKHEF (the National Institute for Nuclear Physics and High Energy Physics, Amsterdam) [21] and at MIT Bates [17,22]. A formalism was developed within a nonrelativistic framework, and calculations of various asymmetries at lower energies were performed in Ref. [23]. The tensor asymmetry has been discussed at higher energies within a Glauber theory approach, with just a central FSI, in Ref. [24].

The paper is organized as follows. First, we establish the general formalism necessary to calculate response functions for polarized targets, and we discuss how to perform these calculations in two different coordinate systems. Then, we continue with the calculation of asymmetries and with the issues presented in using the experimental convention of measuring polarizations along the electron beam direction versus the theoretical choice of polarization axis along the three-momentum transfer $\vec{q}$. In the next section, we present our numerical results, in a kinematic region relevant to experiments at Jefferson Lab. We show both momentum distributions and angular distributions, and we discuss the contributions of the various spin-dependent parts of the final state interactions, as well as the influence of the ground-state wave function. We conclude with a brief summary.

II. FORMALISM

A. Differential cross section

The standard coordinate systems used to describe the ^{2}H$(e,e'p)$ reaction are shown in Fig. 1. The initial and final electron momenta $\boldsymbol{k}$ and $\boldsymbol{k}'$ define the electron scattering plane and the xyz-coordinate system is defined such that the z axis, the quantization axis, lies along the momentum of the virtual photon q, with the x axis in the electron scattering plane and the y axis perpendicular to the plane. The momentum p of the outgoing proton is in general not in this plane and is located relative to the xyz system by the polar angle θ_p and the azimuthal angle ϕ_p. A second coordinate system $x'y'z'$ is chosen such that the z' axis is parallel to the z axis, the x' axis lies in the plane formed by $\boldsymbol{p}$ and $\boldsymbol{q}$, and the y' axis is normal to this plane.

The general form of the ^{2}H$(e,e'p)$ cross section can be written in the laboratory frame as [25,26]

$$\left(\frac{d\sigma^5}{d\epsilon' d\Omega_e d\Omega_p}\right)_h = \frac{m_p m_n p_p}{8\pi^3 M_d}\sigma_{\rm Mott} f_{\rm rec}^{-1}[v_L R_L + v_T R_T + v_{TT} R_{TT} + v_{LT} R_{LT} + h v_{LT'} R_{LT'} + h v_{T'} R_{T'}], \quad (1)$$

where M_d, m_p, and m_n are the masses of the deuteron, proton, and neutron, $p_p = p_1$ and Ω_p are the momentum and solid angle of the ejected proton, ϵ' is the energy of the detected electron, and Ω_e is its solid angle, with $h = \pm 1$ for positive and negative electron helicity. The Mott cross section is

$$\sigma_{\rm Mott} = \left(\frac{\alpha\cos(\theta_e/2)}{2\varepsilon\sin^2(\theta_e/2)}\right)^2, \quad (2)$$

and the recoil factor is given by

$$f_{\rm rec} = \left|1 + \frac{\omega p_p - E_p q\cos\theta_p}{M_d p_p}\right|. \quad (3)$$

The leptonic coefficients v_K are

$$v_L = \frac{Q^4}{q^4}, \quad (4)$$

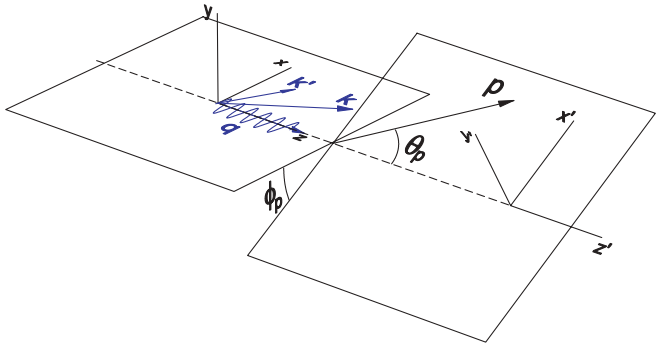

FIG. 1. (Color online) Coordinate systems for the ^{2}H$(e,e'p)$ reaction. k and k' are the initial and final electron four-momenta, q is the four-momentum of the virtual photon, and p is the four-momentum of the final state proton.

$$v_T = \frac{Q^2}{2q^2} + \tan^2\frac{\theta_e}{2}, \quad (5)$$

$$v_{TT} = -\frac{Q^2}{2q^2}, \quad (6)$$

$$v_{LT} = -\frac{Q^2}{\sqrt{2}q^2}\sqrt{\frac{Q^2}{q^2} + \tan^2\frac{\theta_e}{2}}, \quad (7)$$

$$v_{LT'} = -\frac{Q^2}{\sqrt{2}q^2}\tan\frac{\theta_e}{2}, \quad (8)$$

$$v_{T'} = \tan\frac{\theta_e}{2}\sqrt{\frac{Q^2}{q^2} + \tan^2\frac{\theta_e}{2}}. \quad (9)$$

Within this general framework, we have two options for evaluating the response functions. First, we will give expressions for the response functions in terms of matrix elements that are defined with respect to the electron plane, i.e., the xyz plane. These matrix elements are implicitly dependent on ϕ_p, the angle between the hadron plane and electron plane, and these are the responses used, e.g.. in Ref. [25]. Second, we give expressions for the responses in the $x'y'z'$ plane. All quantities given relative to the $x'y'z'$ coordinate system are denoted by a line over the quantity. The current matrix elements, and therefore the response functions, in the $x'y'z'$ coordinate system do not have any ϕ_p dependence. It is much more practical to evaluate the responses in the $x'y'z'$ coordinate system. The commonly used responses in the xyz system can then easily be obtained by accounting for the ϕ_p dependence explicitly [see Eq. (17) below], instead of newly evaluating matrix elements for each value of ϕ_p.

Note that both coordinate systems use the same quantization axis: the z axis and the z' axis are parallel. We will discuss the use of a different polarization along the beam, as commonly done by experimentalists, in the next subsection on asymmetries.

The hadronic tensor for scattering from polarized deuterons is defined as

$$w_{\lambda'_\gamma,\lambda_\gamma}(D) = \sum_{s_1,s_2,\lambda_d,\lambda'_d} \langle \boldsymbol{p}_1 s_1; \boldsymbol{p}_2 s_2; (-)|J_{\lambda'_\gamma}|\boldsymbol{P}\lambda'_d\rangle^* \times \langle \boldsymbol{p}_1 s_1; \boldsymbol{p}_2 s_2; (-)|J_{\lambda_\gamma}|\boldsymbol{P}\lambda_d\rangle \rho_{\lambda_d\lambda'_d}, \quad (10)$$

where

$$J_{\pm 1} = \mp\frac{1}{\sqrt{2}}(J^1 \pm J^2), \quad (11)$$

and

$$J_0 = J^0 \quad (12)$$

is the charge operator. The notation $(-)$ in the final state indicates that the state satisfies the boundary conditions appropriate for an "out" state. The deuteron density matrix

in the xyz frame is

$$\boldsymbol{\rho} = \frac{1}{3}\begin{pmatrix} 1+\sqrt{\frac{3}{2}}T_{10}+\frac{1}{\sqrt{2}}T_{20} & -\sqrt{\frac{3}{2}}(T_{11}^{*}+T_{21}^{*}) & \sqrt{3}T_{22}^{*} \\ -\sqrt{\frac{3}{2}}(T_{11}+T_{21}) & 1-\sqrt{2}T_{20} & -\sqrt{\frac{3}{2}}(T_{11}^{*}-T_{21}^{*}) \\ \sqrt{3}T_{22} & -\sqrt{\frac{3}{2}}(T_{11}-T_{21}) & 1-\sqrt{\frac{3}{2}}T_{10}+\frac{1}{\sqrt{2}}T_{20} \end{pmatrix}, \tag{13}$$

and the set of tensor polarization coefficients is defined as

$$D = \{U, T_{10}, T_{11}, T_{20}, T_{21}, T_{22}\}, \tag{14}$$

with U designating the contribution from unpolarized deuterons. The derivation of the density matrix and the conventions used are described in the Appendix.

The response functions in the xyz frame are given by

$$\begin{aligned} R_L(D) &= w_{00}(D), \\ R_T(D) &= w_{11}(D) + w_{-1-1}(D), \\ R_{TT}(D) &= 2\mathrm{Re}(w_{1-1}(D)), \\ R_{LT}(D) &= -2\mathrm{Re}(w_{01}(D) - w_{0-1}(D)), \\ R_{LT'}(D) &= -2\mathrm{Re}(w_{01}(D) + w_{0-1}(D)), \\ R_{T'}(D) &= w_{11}(D) - w_{-1-1}(D). \end{aligned} \tag{15}$$

Now we proceed to write expressions for the responses in the $x'y'z'$ coordinate system. Calculating the responses in this system offers a faster alternative to the above calculation, which requires a new evaluation of the current matrix elements for each ϕ_p value. The response functions defined above are implicitly dependent upon the angle ϕ_p between the electron plane and the hadron plane containing the proton and neutron in the final state. This dependence can be made explicit by noting that

$$\begin{aligned} &\langle \boldsymbol{p}_1 s_1; \boldsymbol{p}_2 s_2; (-)|J_{\lambda_\gamma}|\boldsymbol{P}\lambda_d\rangle \\ &\quad = e^{i(\lambda_d+\lambda_\gamma-s_1-s_2)\phi_p}\overline{\langle \boldsymbol{p}_1 s_1; \boldsymbol{p}_2 s_2; (-)|J_{\lambda_\gamma}|\boldsymbol{P}\lambda_d\rangle}, \end{aligned} \tag{16}$$

where the line over the matrix elements is used to indicate that they are quantized relative to the $x'y'z'$ coordinate system. The hadronic tensor can then be written as

$$w_{\lambda'_\gamma,\lambda_\gamma}(D) = e^{-i(\lambda'_\gamma-\lambda_\gamma)\phi_p}\overline{w}_{\lambda'_\gamma,\lambda_\gamma}(\overline{D}), \tag{17}$$

where

$$\begin{aligned} \overline{w}_{\lambda'_\gamma,\lambda_\gamma}(\overline{D}) = \sum_{s_1,s_2,\lambda_d,\lambda'_d} &\overline{\langle \boldsymbol{p}_1 s_1; \boldsymbol{p}_2 s_2; (-)|J_{\lambda'_\gamma}|\boldsymbol{P}\lambda'_d\rangle}^{*} \\ &\times \overline{\langle \boldsymbol{p}_1 s_1; \boldsymbol{p}_2 s_2; (-)|J_{\lambda_\gamma}|\boldsymbol{P}\lambda_d\rangle}\,\overline{\rho}_{\lambda_d\lambda'_d}, \end{aligned} \tag{18}$$

and

$$\overline{\rho}_{\lambda_d\lambda'_d} = e^{i(\lambda_d-\lambda'_d)\phi_p}\rho^{D}_{\lambda_d\lambda'_d} \tag{19}$$

is the density matrix defined relative to the $x'y'z'$ coordinate system.

Using Eq. (17) and the definition of the responses in the xyz system, Eq. (15), the response functions in the $x'y'z'$ system then become

$$\begin{aligned} R_L(\overline{D}) &= \overline{R}_L^{(I)}(\overline{D}), \\ R_T(\overline{D}) &= \overline{R}_T^{(I)}(\overline{D}), \\ R_{TT}(\overline{D}) &= \overline{R}_{TT}^{(I)}(\overline{D})\cos 2\phi_p + \overline{R}_{TT}^{(II)}(\overline{D})\sin 2\phi_p, \\ R_{LT}(\overline{D}) &= \overline{R}_{LT}^{(I)}(\overline{D})\cos\phi_p + \overline{R}_{LT}^{(II)}(\overline{D})\sin\phi_p, \\ R_{LT'}(\overline{D}) &= \overline{R}_{LT'}^{(I)}(\overline{D})\sin\phi_p + \overline{R}_{LT'}^{(II)}(\overline{D})\cos\phi_p, \\ R_{T'}(\overline{D}) &= \overline{R}_{T'}^{(II)}(\overline{D}), \end{aligned} \tag{20}$$

where the reduced response functions for the classes I and II are defined in terms of the hadronic tensors as

$$\begin{aligned} \overline{R}_L^{(I)}(\overline{D}) &= \sum_i \overline{R}_L^{(I)}\big(\boldsymbol{\tau}_i^{(I)}\big)\overline{T}_i^{(I)} = \overline{w}_{00}(\overline{D}), \\ \overline{R}_T^{(I)}(\overline{D}) &= \sum_i \overline{R}_T^{(I)}\big(\boldsymbol{\tau}_i^{(I)}\big)\overline{T}_i^{(I)} = \overline{w}_{1,1}(\overline{D}) + \overline{w}_{-1,-1}(\overline{D}), \\ \overline{R}_{TT}^{(I)}(\overline{D}) &= \sum_i \overline{R}_{TT}^{(I)}\big(\boldsymbol{\tau}_i^{(I)}\big)\overline{T}_i^{(I)} = 2\mathrm{Re}(\overline{w}_{1,-1}(\overline{D})), \\ \overline{R}_{TT}^{(II)}(\overline{D}) &= \sum_i \overline{R}_{TT}^{(II)}\big(\boldsymbol{\tau}_i^{(II)}\big)\overline{T}_i^{(II)} = 2\mathrm{Im}(\overline{w}_{1,-1}(\overline{D})), \\ \overline{R}_{LT}^{(I)}(\overline{D}) &= \sum_i \overline{R}_{LT}^{(I)}\big(\boldsymbol{\tau}_i^{(I)}\big)\overline{T}_i^{(I)} = -2\mathrm{Re}(\overline{w}_{01}(\overline{D}) - \overline{w}_{0-1}(\overline{D})), \\ \overline{R}_{LT}^{(II)}(\overline{D}) &= \sum_i \overline{R}_{LT}^{(II)}\big(\boldsymbol{\tau}_i^{(II)}\big)\overline{T}_i^{(II)} = 2\mathrm{Im}(\overline{w}_{01}(\overline{D}) + \overline{w}_{0-1}(\overline{D})), \\ \overline{R}_{LT'}^{(I)}(\overline{D}) &= \sum_i R_{LT'}^{(I)}\big(\boldsymbol{\tau}_i^{(I)}\big)\overline{T}_i^{(I)} = 2\mathrm{Im}(\overline{w}_{01}(\overline{D}) - \overline{w}_{0-1}(\overline{D})), \\ R_{LT'}^{(II)}(\overline{D}) &= \sum_i \overline{R}_{LT'}^{(II)}\big(\boldsymbol{\tau}_i^{(II)}\big)\overline{T}_i^{(II)} = -2\mathrm{Re}(\overline{w}_{01}(\overline{D}) + \overline{w}_{0-1}(\overline{D})), \\ \overline{R}_{T'}^{(II)}(\overline{D}) &= \sum_i \overline{R}_{T'}^{(II)}\big(\boldsymbol{\tau}_i^{(II)}\big)\overline{T}_i^{(II)} = \overline{w}_{1,1}(\overline{D}) - \overline{w}_{-1,-1}(\overline{D}), \end{aligned} \tag{21}$$

where

$$\begin{aligned} \overline{T}_i^{(I)} &\in \{U, \mathrm{Im}(\overline{T}_{11}), \overline{T}_{20}, \mathrm{Re}(\overline{T}_{21}), \mathrm{Re}(\overline{T}_{22})\}, \\ \overline{T}_i^{(II)} &\in \{\overline{T}_{10}, \mathrm{Re}(\overline{T}_{11}), \mathrm{Im}(\overline{T}_{21}), \mathrm{Im}(\overline{T}_{22})\}, \end{aligned} \tag{22}$$

and

$$\begin{aligned} \boldsymbol{\tau}_i^{(I)} &\in \big\{\mathbf{1}, \boldsymbol{\tau}_{11}^{\mathrm{Im}}, \boldsymbol{\tau}_{20}, \boldsymbol{\tau}_{21}^{\mathrm{Re}}, \boldsymbol{\tau}_{22}^{\mathrm{Re}}\big\}, \\ \boldsymbol{\tau}_i^{(II)} &\in \big\{\boldsymbol{\tau}_{10}, \boldsymbol{\tau}_{11}^{\mathrm{Re}}, \boldsymbol{\tau}_{21}^{\mathrm{Im}}, \boldsymbol{\tau}_{22}^{\mathrm{Im}}\big\}. \end{aligned} \tag{23}$$

The τ matrices are defined by Eqs. (A20), (A28), and (A29). The type I and II response functions can be obtained directly by noting that the density matrix can be written as

$$\overline{\boldsymbol{\rho}} = \frac{1}{3}\left(\mathbf{1} + \sum_i \boldsymbol{\tau}_i^{(I)}\overline{T}_i^{(I)} + \sum_i \boldsymbol{\tau}_i^{(II)}\overline{T}_i^{(II)}\right). \tag{24}$$

Defining a set of projected hadronic tensors as

$$\overline{w}_{\lambda'_\gamma,\lambda_\gamma}\left(\boldsymbol{\tau}_i^{(I,II)}\right) = \frac{1}{3}\sum_{s_1,s_2,\lambda_d,\lambda'_d} \overline{\langle \boldsymbol{p}_1 s_1; \boldsymbol{p}_2 s_2; (-)|J_{\lambda'_\gamma}|\boldsymbol{P}\lambda'_d\rangle}^{*} \times \overline{\langle \boldsymbol{p}_1 s_1; \boldsymbol{p}_2 s_2; (-)|J_{\lambda_\gamma}|\boldsymbol{P}\lambda_d\rangle}\left(\boldsymbol{\tau}_i^{(I,II)}\right)_{\lambda_d\lambda'_d}, \tag{25}$$

the type I and II response functions are then obtained by replacing the hadronic tensors on the right-hand side of the expressions in Eq. (21) with each appropriate projected hadronic tensor in turn. Note that the τ matrices satisfy

$$\left(\boldsymbol{\tau}_i^{(I)}\right)_{-\lambda-\lambda'} = (-1)^M\left(\boldsymbol{\tau}_i^{(I)}\right)_{\lambda\lambda'}, \tag{26}$$

and

$$\left(\boldsymbol{\tau}_i^{(II)}\right)_{-\lambda-\lambda'} = (-1)^{M+1}\left(\boldsymbol{\tau}_i^{(II)}\right)_{\lambda\lambda'}. \tag{27}$$

B. Symmetries of the current matrix elements

The current matrix elements used here are defined in Ref. [7]. The matrix elements quantized in the hadron plane $x'y'z'$ can be shown to satisfy the symmetry

$$\overline{\langle \boldsymbol{p}_1 s_1; \boldsymbol{p}_2 s_2; (-)|J_{\lambda_\gamma}|\boldsymbol{P}\lambda_d\rangle} = (-1)^{\lambda_\gamma+\lambda_d-s_1-s_2}\overline{\langle \boldsymbol{p}_1 - s_1; \boldsymbol{p}_2 - s_2; (-)|J_{\lambda_\gamma}|\boldsymbol{P} - \lambda_d\rangle} \tag{28}$$

by starting with

$$i\Sigma_2\gamma^0 u(\overline{\boldsymbol{p}}, s) = (-1)^{\frac{1}{2}+s}u(\overline{\boldsymbol{p}}, -s), \tag{29}$$

which relies on the fact that the nucleon momenta have, by construction, no y' component when quantized in the hadron plane.

Application of parity and time reversal to these matrix elements requires that

$$\langle \boldsymbol{p}_1 s_1; \boldsymbol{p}_2 s_2; (-)|J_{\lambda_\gamma}|\boldsymbol{P}\lambda_d\rangle = (-1)^{\lambda_\gamma+\lambda_d-s_1-s_2}\langle \boldsymbol{P} - \lambda_d|J_{\lambda_\gamma}|\boldsymbol{p}_1 - s_1; \boldsymbol{p}_2 - s_2; (+)\rangle. \tag{30}$$

Combining this with Eq. (28) gives

$$\overline{\langle \boldsymbol{p}_1 s_1; \boldsymbol{p}_2 s_2; (-)|J_{\lambda_\gamma}|\boldsymbol{P}\lambda_d\rangle} = \overline{\langle \boldsymbol{P}\lambda_d|J_{\lambda_\gamma}|\boldsymbol{p}_1 s_1; \boldsymbol{p}_2 s_2; (+)\rangle} = \overline{\langle \boldsymbol{p}_1 s_1; \boldsymbol{p}_2 s_2; (+)|J_{\lambda_\gamma}|\boldsymbol{P}\lambda_d\rangle}^{*}. \tag{31}$$

In the plane-wave approximation, there is no difference between the $(-)$ and $(+)$ boundary conditions. So in this approximation, the current matrix elements are real.

C. Asymmetries

The simple form of Eq. (1) is due to the choice of quantization axis associated with the plane determined by the virtual photon momentum and the ejectile momentum. In practice, the polarization coefficients are determined relative to a coordinate system fixed in the laboratory with the axis of quantization along the electron beam momentum. This can be easily accommodated by rotating the density matrix. The relationship between the density matrix in the $x'y'z'$ coordinate system and the system with the quantization axis z'' along the electron momentum $\boldsymbol{k}$ and with y'' parallel to y is

$$\overline{\rho}_{\lambda_d\lambda'_d} = \sum_{\Lambda\Lambda'} D^1_{\lambda_d\Lambda}(-\phi_p, \theta_{kq}, 0)D^1_{\lambda'_d\Lambda'}(-\phi_p, \theta_{kq}, 0)\tilde{\rho}^D_{\Lambda\Lambda'}, \tag{32}$$

where the tilde denotes the density matrix for the $x''y''z''$ coordinate system, and θ_{kq} is the angle between the beam momentum $\boldsymbol{k}$ and the momentum transfer $\boldsymbol{q}$. The polarization coefficients $\overline{T}_{JM}$ can be found as functions of the $\widetilde{T}_{JM}$ by using

$$\begin{aligned} \overline{T}_{J0} &= \mathrm{Tr}(\boldsymbol{\tau}^\dagger_{J0}\overline{\boldsymbol{\rho}}), \\ \mathrm{Re}(\overline{T}_{JM}) &= \tfrac{1}{2}\mathrm{Tr}\left[\boldsymbol{\tau}^{\mathrm{Re}\,\dagger}_{JM}\overline{\boldsymbol{\rho}}\right], \\ \mathrm{Im}(\overline{T}_{JM}) &= \tfrac{1}{2}\mathrm{Tr}\left[\boldsymbol{\tau}^{\mathrm{Im}\,\dagger}_{JM}\overline{\boldsymbol{\rho}}\right]. \end{aligned} \tag{33}$$

The response functions for the $x''y''z''$ coordinate system can by found by using these in Eq. (21).

The asymmetries that we will calculate here involve the case where $\widetilde{T}_{10}$ is nonzero with all other polarization coefficients equal to zero, or where $\widetilde{T}_{20}$ is nonzero with all other polarization coefficients equal to zero. In the first case,

$$\begin{aligned} \overline{T}_{10} &= \cos\theta_{kq}\widetilde{T}_{10}, \\ \mathrm{Re}(\overline{T}_{11}) &= -\frac{1}{\sqrt{2}}\sin\theta_{kq}\cos\phi_p\widetilde{T}_{10}, \\ \mathrm{Im}(\overline{T}_{11}) &= \frac{1}{\sqrt{2}}\sin\theta_{kq}\sin\phi_p\widetilde{T}_{10}, \\ \overline{T}_{2M} &= 0, \end{aligned} \tag{34}$$

while in the second case,

$$\begin{aligned} \overline{T}_{1M} &= 0, \\ \overline{T}_{20} &= \frac{1}{4}(1 + 3\cos 2\theta_{kq})\widetilde{T}_{20}, \\ \mathrm{Re}(\overline{T}_{21}) &= -\sqrt{\frac{3}{8}}\sin 2\theta_{kq}\cos\phi_p\widetilde{T}_{20}, \\ \mathrm{Im}(\overline{T}_{21}) &= \sqrt{\frac{3}{8}}\sin 2\theta_{kq}\sin\phi_p\widetilde{T}_{20}, \\ \mathrm{Re}(\overline{T}_{22}) &= \sqrt{\frac{3}{32}}(1 - \cos 2\theta_{kq})\cos 2\phi_p\widetilde{T}_{20}, \\ \mathrm{Im}(\overline{T}_{22}) &= -\sqrt{\frac{3}{32}}(1 - \cos 2\theta_{kq})\sin 2\phi_p\widetilde{T}_{20}. \end{aligned} \tag{35}$$

A similar relation between the xyz and $x''y''z''$ coordinates systems is given by

$$\rho_{\lambda_d\lambda'_d} = \sum_{\Lambda\Lambda'} d^1_{\lambda_d\Lambda}(\theta_{kq})d^1_{\lambda'_d\Lambda'}(\theta_{kq})\tilde{\rho}^D_{\Lambda\Lambda'}. \tag{36}$$

Then,

$$T_{JM} = T_{JM}(\widetilde{D}). \tag{37}$$

The relations between the polarization coefficients can be obtained from Eqs. (34) and (35) by setting $\phi_p = 0$ and making the replacements $\overline{T}_{JM} \to T_{JM}$.

The single and double asymmetries for these two polarizations are defined as

$$\begin{aligned}
A_d^V &= \frac{v_L R_L(\widetilde{T}_{10}) + v_T R_T(\widetilde{T}_{10}) + v_{TT} R_{TT}(\widetilde{T}_{10}) + v_{LT} R_{LT}(\widetilde{T}_{10})}{\widetilde{T}_{10}\Sigma}, \\
A_d^T &= \frac{v_L R_L(\widetilde{T}_{20}) + v_T R_T(\widetilde{T}_{20}) + v_{TT} R_{TT}(\widetilde{T}_{20}) + v_{LT} R_{LT}(\widetilde{T}_{20})}{\widetilde{T}_{20}\Sigma}, \\
A_{\rm ed}^V &= \frac{v_{LT'} R_{LT'}(\widetilde{T}_{10}) + v_{T'} R_{T'}(\widetilde{T}_{10})}{\widetilde{T}_{10}\Sigma}, \\
A_{\rm ed}^T &= \frac{v_{LT'} R_{LT'}(\widetilde{T}_{20}) + v_{T'} R_{T'}(\widetilde{T}_{20})}{\widetilde{T}_{20}\Sigma},
\end{aligned} \tag{38}$$

where

$$\Sigma = v_L R_L(U) + v_T R_T(U) + v_{TT} R_{TT}(U) + v_{LT} R_{LT}(U). \tag{39}$$

Here $R_i(\widetilde{T}_{10})$ and $R_i(\widetilde{T}_{20})$ denote the response functions where only $\widetilde{T}_{10}$ is nonzero or only $\widetilde{T}_{20}$ is nonzero. $R_i(U)$ denotes the unpolarized response functions.

Using the definitions of the asymmetries, the expressions for the $\overline{T}_{JM}$ as a function of the $\widetilde{T}$, and the definitions of the response functions in the $x'y'z'$ system, one obtains the following symmetry relations with respect to ϕ_p:

$$\begin{aligned}
A_d^V(\phi_p) &= -A_d^V(360^\circ - \phi_p), \\
A_d^T(\phi_p) &= A_d^T(360^\circ - \phi_p), \\
A_{\rm ed}^V(\phi_p) &= A_{\rm ed}^V(360^\circ - \phi_p), \\
A_{\rm ed}^T(\phi_p) &= -A_{\rm ed}^T(360^\circ - \phi_p).
\end{aligned} \tag{40}$$

D. Current matrix elements

A detailed description of the impulse approximation current matrix elements used here is presented in Ref. [7]. These matrix elements are constructed based on the covariant spectator approximation [27]. A relativistic wave function [8] and NN scattering data [9] are used for our calculation of the full, spin-dependent final state interactions. The main difference from many other high quality calculations using the generalized eikonal approximation [10–12] or a diagrammatic approach [13] is the inclusion of all the spin-dependent pieces in the nucleon-nucleon amplitude. Full FSIs have recently been included in Ref. [14].

To construct the scattering amplitudes needed for the calculation of the FSIs, we start with np helicity matrices extracted from SAID [9]. The on-shell scattering amplitudes can be given in terms of five Fermi invariants as

$$\begin{aligned}
M_{ab;cd} = {} & \mathcal{F}_S(s,t)\delta_{\rm ac}\delta_{\rm bd} + \mathcal{F}_V(s,t)\gamma_{\rm ac}\cdot\gamma_{\rm bd} \\
& + \mathcal{F}_T(s,t)\sigma_{\rm ac}^{\mu\nu}(\sigma_{\mu\nu})_{\rm bd} + \mathcal{F}_P(s,t)\gamma_{\rm ac}^5\gamma_{\rm bd}^5 \\
& + \mathcal{F}_A(s,t)(\gamma^5\gamma)_{\rm ac}\cdot(\gamma^5\gamma)_{\rm bd},
\end{aligned} \tag{41}$$

where s and t are the usual Mandelstam variables. The Fermi invariants are then determined using the helicity amplitudes. A table of the invariant functions is constructed in terms of s and the center-of-momentum angle θ. The table is then interpolated to obtain the invariant functions at the values required by the integration.

To estimate the possible effects of this contribution to the current matrix elements, we use a simple prescription for the off-shell behavior of the amplitude. Although additional invariants are possible when the nucleon is allowed to go off-shell, we keep only the forms in Eq. (41). The center-of-momentum angle is calculated using

$$\cos\theta = \frac{t-u}{\sqrt{s-4m^2}\sqrt{\frac{(4m^2-t-u)^2}{s} - 4m^2}}. \tag{42}$$

The invariants are then replaced by

$$\mathcal{F}_i(s,t) \to \mathcal{F}_i(s,t,u)F_N(s+t+u-3m^2), \tag{43}$$

where

$$F_N(p^2) = \frac{\left(\Lambda_N^2 - m^2\right)^2}{(p^2-m^2)^2 + \left(\Lambda_N^2 - m^2\right)^2}, \tag{44}$$

and the $\mathcal{F}_i(s,t,u)$ are obtained from interpolation of the on-shell invariant functions with the center-of-momentum angle obtained from Eq. (42). The form factor (44) is used as a cutoff to limit contributions where the nucleon is highly off-shell. We use a value of $\Lambda_N = 1$ GeV in this paper. The numerical effects of variations in the cutoff parameter have been studied in Ref. [7].

III. RESULTS

All results are shown for a quantization axis along the beam direction, as measured in experiments, not along the direction of the three-momentum transfer.

1. *Momentum distributions*

In Fig. 2, we show the four asymmetries for a four-momentum transfer of $Q^2 = 2$ GeV^2 and $x = 1$. These kinematics correspond to quasielastic scattering. Note that in the plane-wave approximation, the asymmetries A_d^V and $A_{\rm ed}^T$ vanish. They are nonzero only when the FSIs are included. This is predicted in nonrelativistic plane-wave impulse approximation (PWIA) calculations, and our relativistic approach does not change this feature. In the cases where the asymmetries are nonzero for PWIA, the inclusion of FSIs leads to a shift, and a slight distortion, of the features that are already present in the asymmetries. The dips and bumps become narrower when FSIs are included, and they appear at somewhat lower missing momenta. The difference between just on-shell FSIs and full FSIs including on-shell and off-shell distributions is very small. The largest off-shell FSI effects are present for larger missing momenta in $A_{\rm ed}^T$.

From our discussion in Sec. II B, we can now explain the observed behavior of the asymmetries in PWIA: all PWIA current matrix elements are real, and so any response that

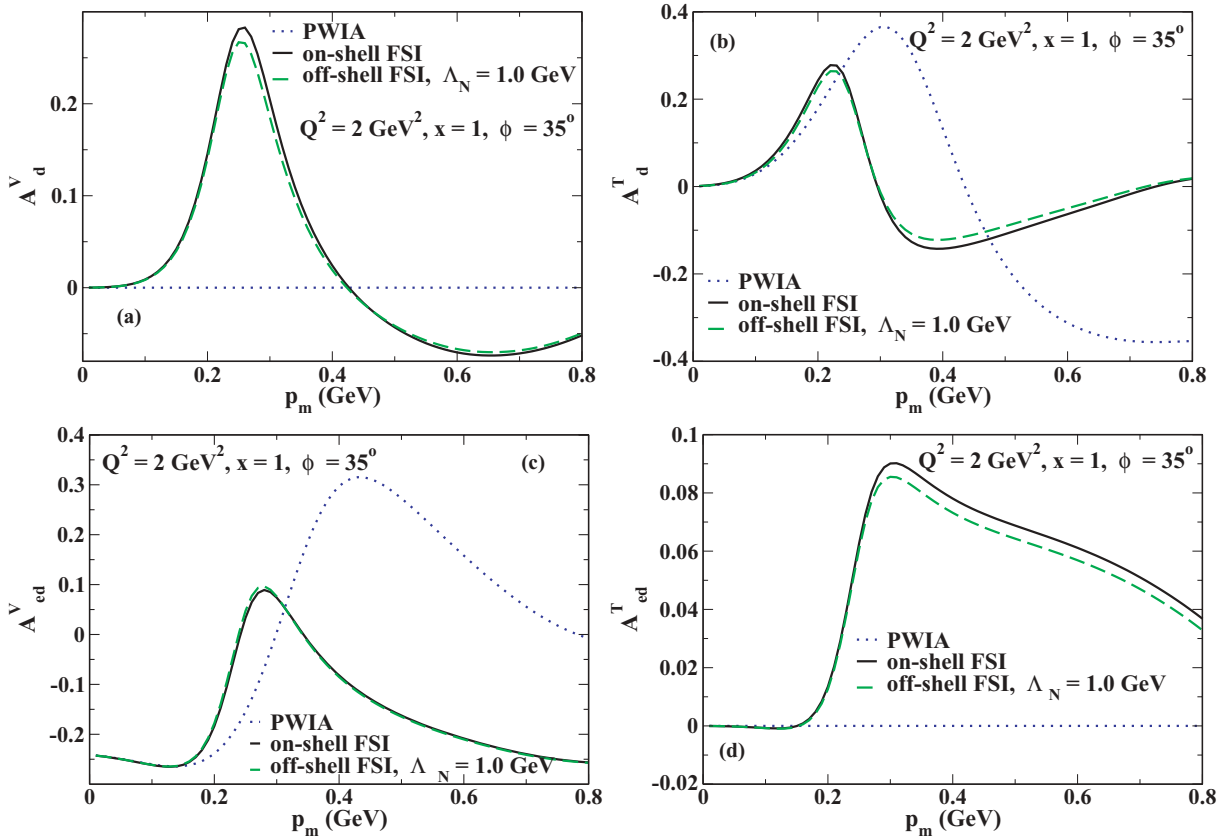

FIG. 2. (Color online) Asymmetries A_d^V (a), A_d^T (b), $A_{\rm ed}^V$ (c), and $A_{\rm ed}^T$ (d) for a beam energy of 5.5 GeV, $Q^2 = 2\,{\rm GeV}^2$, $x = 1$, and $\phi_p = 35^\circ$, are shown calculated in PWIA (dotted line), with on-shell FSI (solid line), and with on-shell and off-shell FSI (dashed line), as a function of the missing momentum.

consists of taking the imaginary part of any part of the hadronic tensor will vanish in PWIA. When consulting Eq. (22), we see that the vector asymmetries with $\bar{T}_{10} \neq 0$ are associated with the class II responses, and that the tensor asymmetries with $\bar{T}_{20} \neq 0$ are associated with the class I responses. From its definition, we can see that A_d^V is associated with the vector, i.e., class II, contributions to the *L, T, TT,* and *LT* responses. The *L* and *T* responses have no class II versions, and the class II versions of the *TT* and *LT* responses are proportional to the imaginary part of certain pieces of the hadronic tensor. Thus, A_d^V vanishes in PWIA. A similar argument shows that $A_{\rm ed}^T$ must vanish in PWIA, whereas the other two asymmetries will always have nonzero contributions. This argument was made in the hadron plane, in the $x'y'z'$ frame. It is also valid when the quantization axis is rotated, as the rotation itself will not lead to a nonzero value for an asymmetry that vanishes for one set of quantization axes.

In Fig. 3, we show the four asymmetries for a four-momentum transfer of $Q^2 = 2$ GeV^2 and $x = 1.3$. These kinematics are away from the quasielastic peak, and we expect off-shell contributions to the FSIs to be more relevant here. We have observed the increase in relative importance of the off-shell FSIs already for unpolarized observables in Ref. [7]. Due to the chosen kinematics, smaller values of the missing momentum are not accessible. As for the quasielastic kinematics shown above, A_d^V and $A_{\rm ed}^T$ are nonzero only after FSIs are included, and the FSIs shift the bumps and dips to lower missing momenta. The shift to lower momenta is much smaller here than for the quasielastic case, though. In contrast to the $x = 1$ kinematics, the off-shell FSIs now play a more prominent role. The differences between just on-shell FSIs and off-shell and on-shell FSIs are large for A_d^V and $A_{\rm ed}^T$, and they are apparent already at low missing momentum. For the two other asymmetries, $A_{\rm ed}^V$ and A_d^T, the differences are less pronounced and are most significant at the largest missing momenta considered here. Having a nonzero asymmetry already in PWIA makes the asymmetry less sensitive to off-shell effects: if the PWIA results are nonzero, the FSIs are very relevant corrections, and the off-shell FSIs are less significant corrections of the correction; if the PWIA results are zero, the FSIs provide the entire asymmetry, and the off-shell FSI corrections are relevant.

The asymmetries that we investigate here also have a dependence on the azimuthal angle ϕ_p of the outgoing proton. The two sets of figures above were shown for a value of $\phi_p = 35^\circ$. This value was chosen to avoid any special cases for $\phi_p = 0^\circ$, 45°, or 90°. However, the overall ϕ_p dependence is interesting, too. We show this dependence for all four asymmetries in Fig. 4 in a three-dimensional plot.

One can see that for A_d^V, the broad bump and dip structures observed for $\phi_p = 35^\circ$ turn into a broad dip and bump for ϕ_p values above 180°, inverting the original, low ϕ_p structure. A

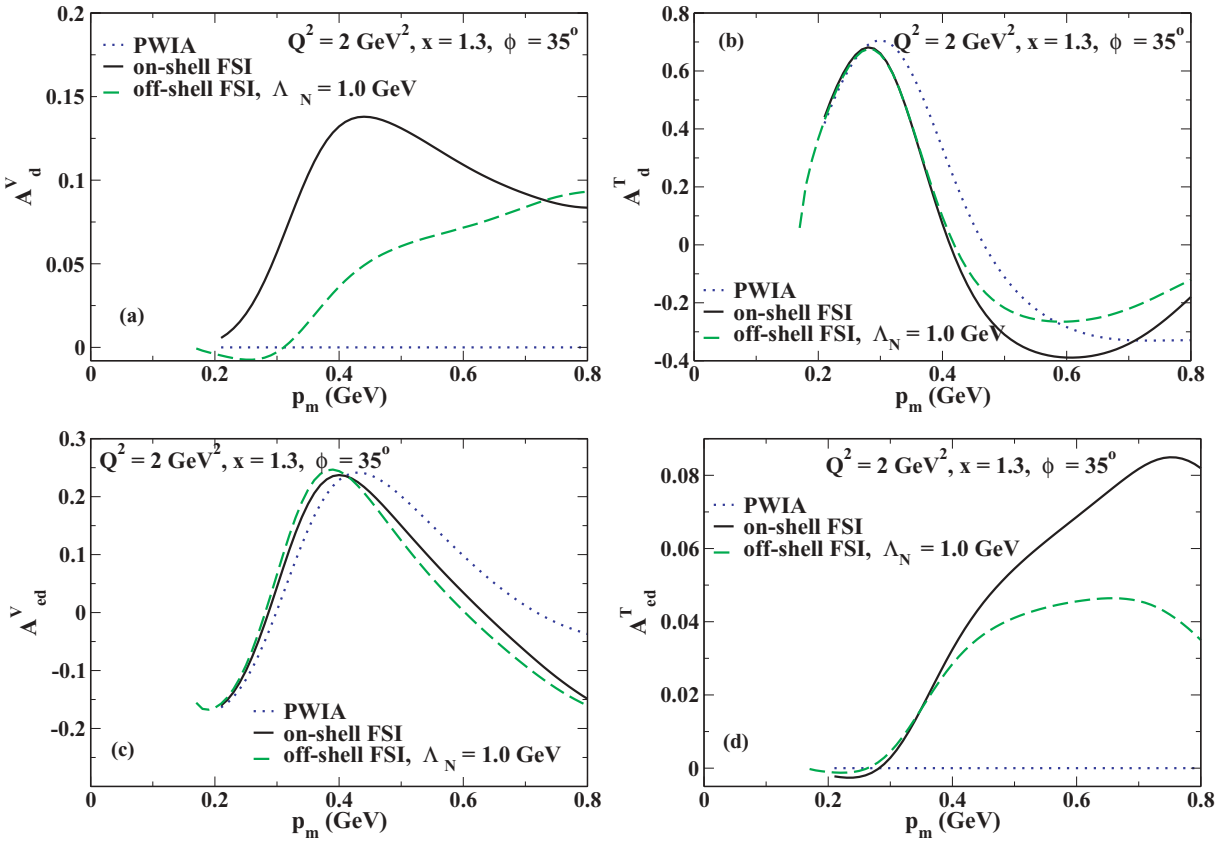

FIG. 3. (Color online) Asymmetries A_d^V (a), A_d^T (b), $A_{\rm ed}^V$ (c), and $A_{\rm ed}^T$ (d) for a beam energy of 5.5 GeV, $Q^2 = 2$ GeV^2, $x = 1.3$, and $\phi_p = 35^\circ$ are shown calculated in PWIA (dotted line), with on-shell FSI (solid line), and with on-shell and off-shell FSI (dashed line), as a function of the missing momentum.

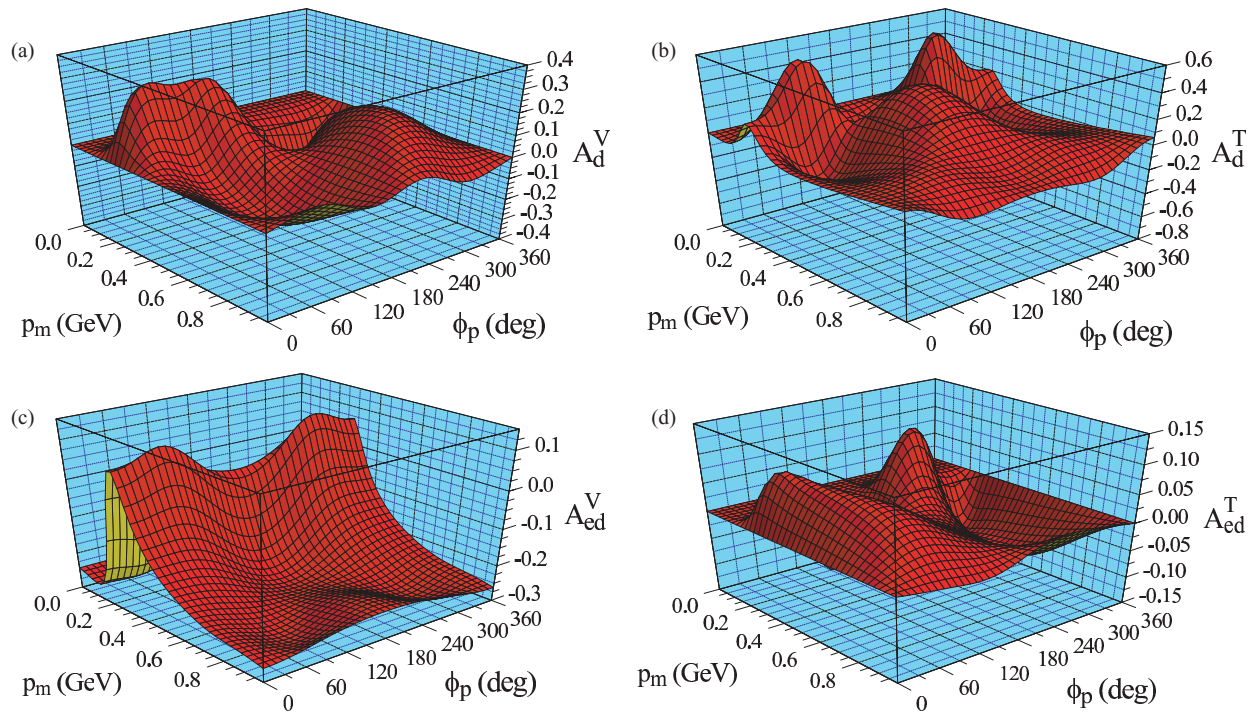

FIG. 4. (Color online) Asymmetries A_d^V (a), A_d^T (b), $A_{\rm ed}^V$ (c), and $A_{\rm ed}^T$ (d), for a beam energy of 5.5 GeV, $Q^2 = 2$ GeV^2, and $x = 1$ are shown calculated with on-shell FSI as a function of the missing momentum and the proton's azimuthal angle.

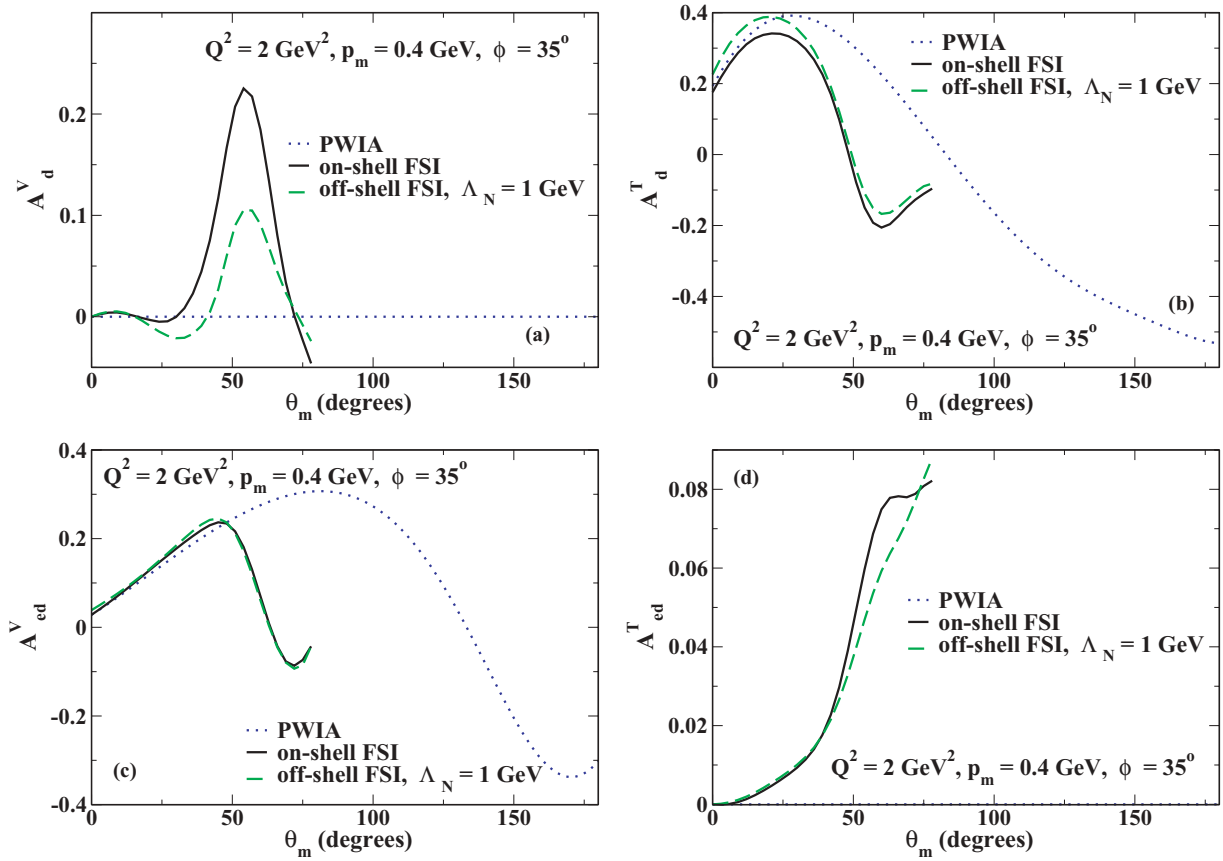

FIG. 5. (Color online) Asymmetries A_d^V (a), A_d^T (b), $A_{\rm ed}^V$ (c), and $A_{\rm ed}^T$ (d) for a beam energy of 5.5 GeV, $Q^2 = 2$ GeV^2, $p_m = 0.4$ GeV, and $\phi_p = 35^\circ$ are shown calculated in PWIA (dotted line), with on-shell FSI (solid line), and with on-shell and off-shell FSI (dashed line), as a function of the polar angle of the missing momentum.

very similar inversion of the structures is observed for $A_{\rm ed}^T$: the broad ridge at lower ϕ_p turns into a valley for large ϕ_p, and the sharp dip at low missing momenta and medium ϕ_p turns into a peak at $\phi_p > 180^\circ$. For the other two asymmetries, A_d^T and $A_{\rm ed}^V$, the plots are symmetric around $\phi_p = 180^\circ$. This is the behavior predicted by Eq. (40) for the four asymmetries.

For the kinematics away from the quasielastic peak, for $x = 1.3$, the same type of ϕ_p dependence and the same ϕ_p symmetries are observed, and we therefore do not display a separate figure. The asymmetries reach much larger maximum values for $x = 1.3$, though.

2. *Angular distributions*

We now discuss our results for angular distributions. Note that for the FSI calculations, there is a limit to the kinematic region in which we can calculate, because the proton-neutron scattering amplitude that we use is available only for pn energies up to 1.3 GeV; see Ref. [7] for details.

In Fig. 5, we show the four asymmetries as functions of the angle for a fixed missing momentum value of $p_m = 0.4$ GeV, and for a fixed $\phi_p = 35^\circ$. The nonrelativistic, factorized PWIA prediction for A_d^T is $A_d^T \propto 1 - 3\cos^2\theta$, which leads to zeros for $\theta = 54.7^\circ$ and $\theta = 125.3^\circ$. If we use only the S-wave and D-wave contributions to the ground-state wave function, and perform the PWIA calculation with the quantization axis along the three-momentum transfer $\vec{q}$, we observe exactly this type of angular dependence. The P-wave contributions lead to slight deviations from the nonrelativistic angular pattern. In our figures, we used a quantization axis along the beam, and this rotation obscures the original structure of the asymmetry. In practice, experimentalists polarize their targets with respect to the beam. The angular dependence of $A_{\rm ed}^V$ even in nonrelativistic PWIA is much more complicated than the structure for A_d^T, because the beam-vector asymmetry $A_{\rm ed}^V$ is equal to the ratio of helicity-dependent and helicity-independent responses. This prevents the cancellations of helicity-independent expressions in numerator and denominator that is present in the tensor asymmetry A_d^T, and causes its simple angular structure. For A_d^V and $A_{\rm ed}^T$, the nonrelativistic result predicts zero for all angles, and this result persists for our fully relativistic calculation, for the reasons discussed above.

Again, we observe the same pattern that was apparent for the momentum distributions: for A_d^T and $A_{\rm ed}^V$, the FSI effects are small for small angles and become important only for larger angles. The differences between on-shell FSI calculations and FSI calculations including off-shell FSIs, too, is very small. For A_d^V and $A_{\rm ed}^T$, the off-shell FSI effects are more pronounced, in particular for A_d^V. Note that when calculating an angular distribution for a fixed missing momentum, we slice through various values of x, and therefore the relative importance of the off-shell FSI contribution is different for different angles θ.

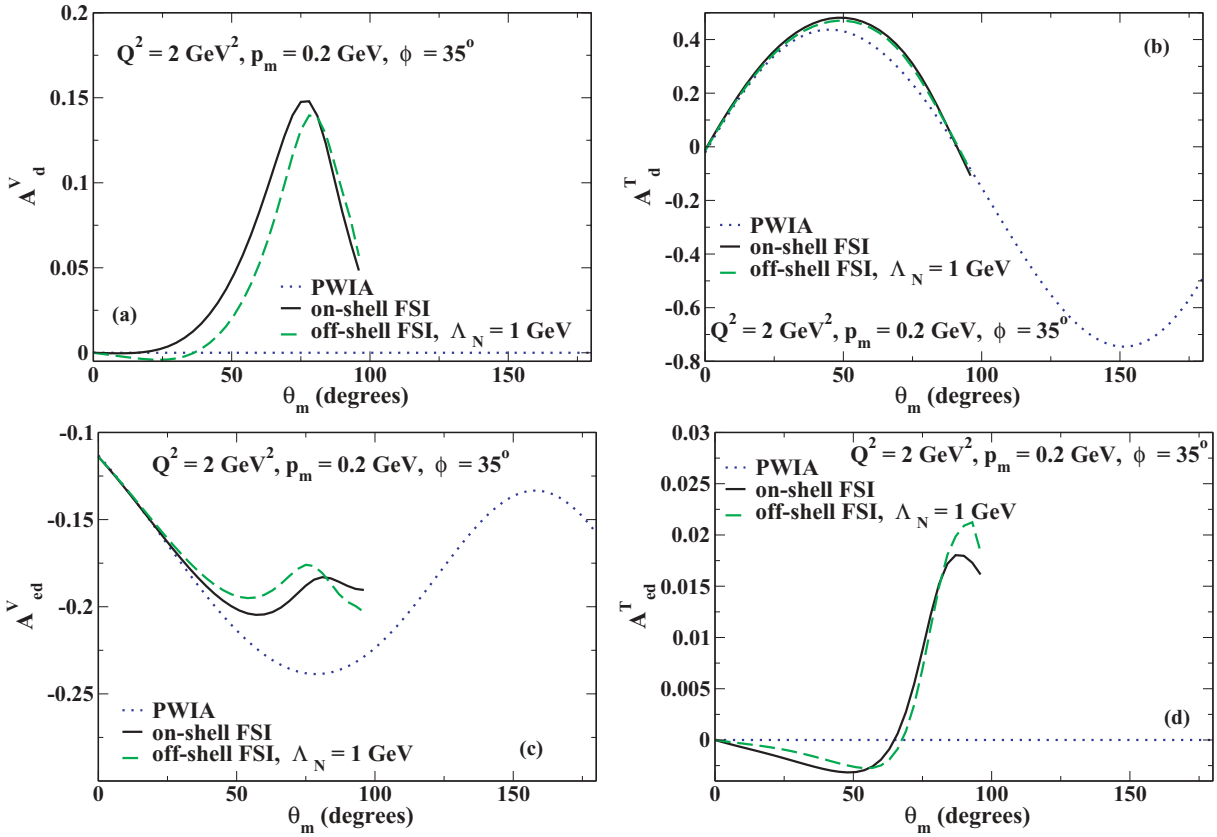

FIG. 6. (Color online) Asymmetries A_d^V (a), A_d^T (b), $A_{\rm ed}^V$ (c), and $A_{\rm ed}^T$ (d) for a beam energy of 5.5 GeV, $Q^2 = 2$ GeV^2, $p_m = 0.2$ GeV, and $\phi_p = 35^\circ$ are shown calculated in PWIA (dotted line), with on-shell FSI (solid line), and with on-shell and off-shell FSI (dashed line), as a function of the polar angle of the missing momentum.

At the four-momentum transfer of 2 GeV^2, we are limited in the range of polar angles θ that we may access, as complete np scattering amplitudes are available only up to 1.3 GeV. The results for $Q^2 = 1$ GeV^2 and otherwise identical kinematics are not qualitatively different from what we see at smaller angles.

We show in Fig. 6 the asymmetries at a lower missing momentum value, $p_m = 0.2$ GeV, as functions of the angle. Overall, it is clear that for the lower missing momentum value, $p_m = 0.2$ GeV, the influence of FSIs is not that large. As before, the asymmetry A_d^V shows an off-shell FSI result that differs from the on-shell FSI for a larger range of angles, but the effect is much less pronounced than for higher p_m. Both $A_{\rm ed}^V$ and $A_{\rm ed}^T$ show small off-shell FSI effects in the region where the asymmetries are large. The off-shell FSI contributions are somewhat limited here, because for $p_m = 0.2$ GeV, the maximum kinematically possible x value is 1.3.

Summarizing, it is interesting to note that the tensor asymmetry A_d^T and the double spin asymmetry $A_{\rm ed}^V$ exhibit rather similar behavior, even though they have quite different structures: the former depends on the helicity-independent terms of the cross section and has a tensor (T_{20}) structure, whereas the latter depends on the helicity-dependent terms of the cross section and has a vector structure (T_{10}). Due to invariance under parity and time reversal, both responses are nonzero in PWIA, and they show similar structures and sensitivity to FSI effects. Their ϕ_p dependence is similar, too, showing a mirror symmetry along $\phi_p = 180^\circ$. In the same way, the target spin asymmetry A_d^V (helicity-independent, vector) and the tensor-beam asymmetry $A_{\rm ed}^T$ (helicity-dependent, tensor) show similar traits: they are both zero in PWIA and are more sensitive even to off-shell FSI effects. Their ϕ_p dependence leads to an inversion of all features above $\phi_p = 180^\circ$.

3. *Contributions from individual parts of the NN scattering amplitude to the FSIs*

In our calculation of the final state interactions, we use the full nucleon-nucleon scattering amplitude. There are several ways to decompose and parametrize the NN scattering amplitude. It can be parametrized with five terms: a central, spin-independent term, a spin-orbit term, and three double spin-flip contributions. It can also be given in terms of invariants, using a scalar, vector, tensor, pseudoscalar, and axial term. Some of these parametrizations may be useful and enlightening in trying to understand what is happening. As we are interested in the effects of target polarization, investigating the effects of spin-dependent terms in the FSIs is a logical and interesting step. We separate the NN amplitudes into a central term, a single spin-flip (i.e., spin-orbit) term, and three double spin-flip terms.

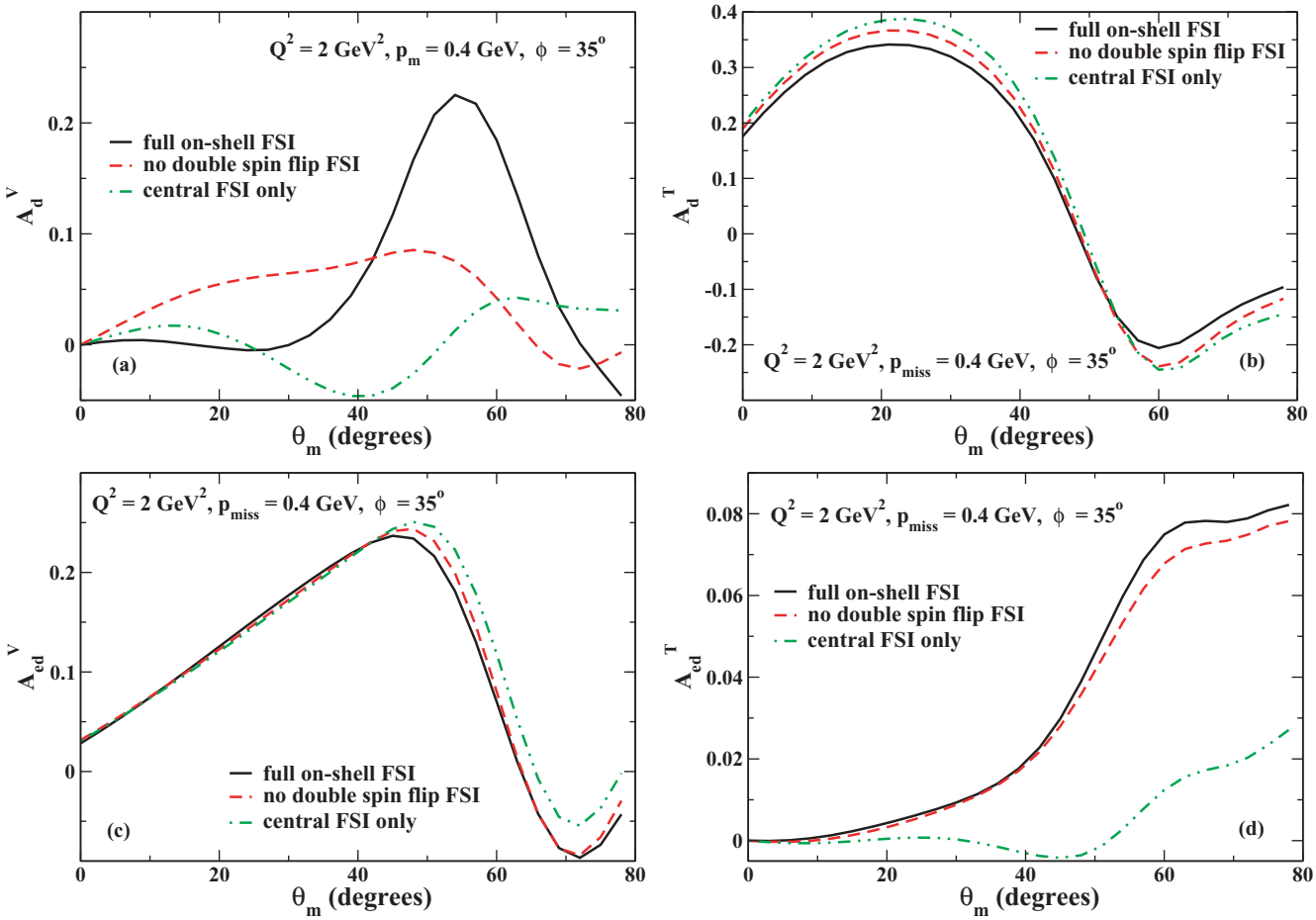

FIG. 7. (Color online) Asymmetries A_d^V (a), A_d^T (b), $A_{\rm ed}^V$ (c), and $A_{\rm ed}^T$ (d) for a beam energy of 5.5 GeV, $Q^2 = 2$ GeV^2, $p_m = 0.4$ GeV, and $\phi_p = 35^\circ$ are shown calculated with on-shell FSI (solid line), without any double spin-flip terms in the on-shell FSI (dashed line), and with central on-shell FSI only (dash-double-dotted line), as a function of the angle θ_m of the missing momentum.

Figure 7 shows the contributions of the central, central and single spin-flip, and full FSIs to the four asymmetries at $Q^2 = 2$ GeV^2 and $p_m = 0.4$ GeV as a function of the angle of the missing momentum. The tensor asymmetry A_d^T shows little sensitivity to the details of the FSIs, it just shows some minor quantitative changes in the dip and peak region. The beam-vector asymmetry $A_{\rm ed}^V$ is insensitive at lower angles, but shows small changes in magnitude at larger angles. In both cases, there is no shape change when the different parts of the FSIs are added. This changes when considering the target-spin asymmetry A_d^V and the tensor-beam asymmetry $A_{\rm ed}^T$. For these asymmetries, the shape is quite different when only the central part of the FSIs is included. The central FSI result for $A_{\rm ed}^T$ is rather small and even takes some negative values in a shallow dip around $\theta \approx 45^\circ$. Once the single spin-flip FSI is included, the asymmetry changes and shows a steep rise with a shallow shoulder at larger angles. With the inclusion of the double spin-flip FSIs, the magnitude of the asymmetry increases a bit at larger angles.

For A_d^V, the influence of the spin-dependent FSIs is most pronounced: while the asymmetry is very small and changes sign twice with central FSIs, the inclusion of the single spin-flip term leads to an asymmetry that is similar in shape, albeit a bit larger than with central FSIs, and of opposite sign. The double spin-flip terms completely change the shape of the asymmetry, leading to a pronounced peak and a much larger maximum value. Here, for A_d^V, the effect of the double spin-flip FSIs is most pronounced and most relevant.

Figure 8 shows the contributions of the central, central and single spin-flip, and full FSIs to the four asymmetries at $Q^2 = 2$ GeV^2 and $x = 1$ as a function of the missing momentum. While the angular distributions for $p_m = 0.4$ GeV shown in Fig. 7 do not show a very pronounced effect of the double spin-flip terms on A_d^T and $A_{\rm ed}^V$, the momentum distribution for A_d^T shows that especially for larger missing momenta, the spin-dependent FSIs are very relevant. Starting for $p_m = 0.4$ GeV, the results without the full spin-dependence deviate significantly from the full FSI result, and for $p_m > 0.5$ GeV, an interesting inversion happens: the result for central FSI only is closer to—but still far from—the full FSI result than the calculation without double spin-flip. This indicates that interference effects are relevant for A_d^T in this kinematic region. For A_d^V, a similar picture emerges for larger missing momentum: for $p_m > 0.4$ GeV, central FSI only results are

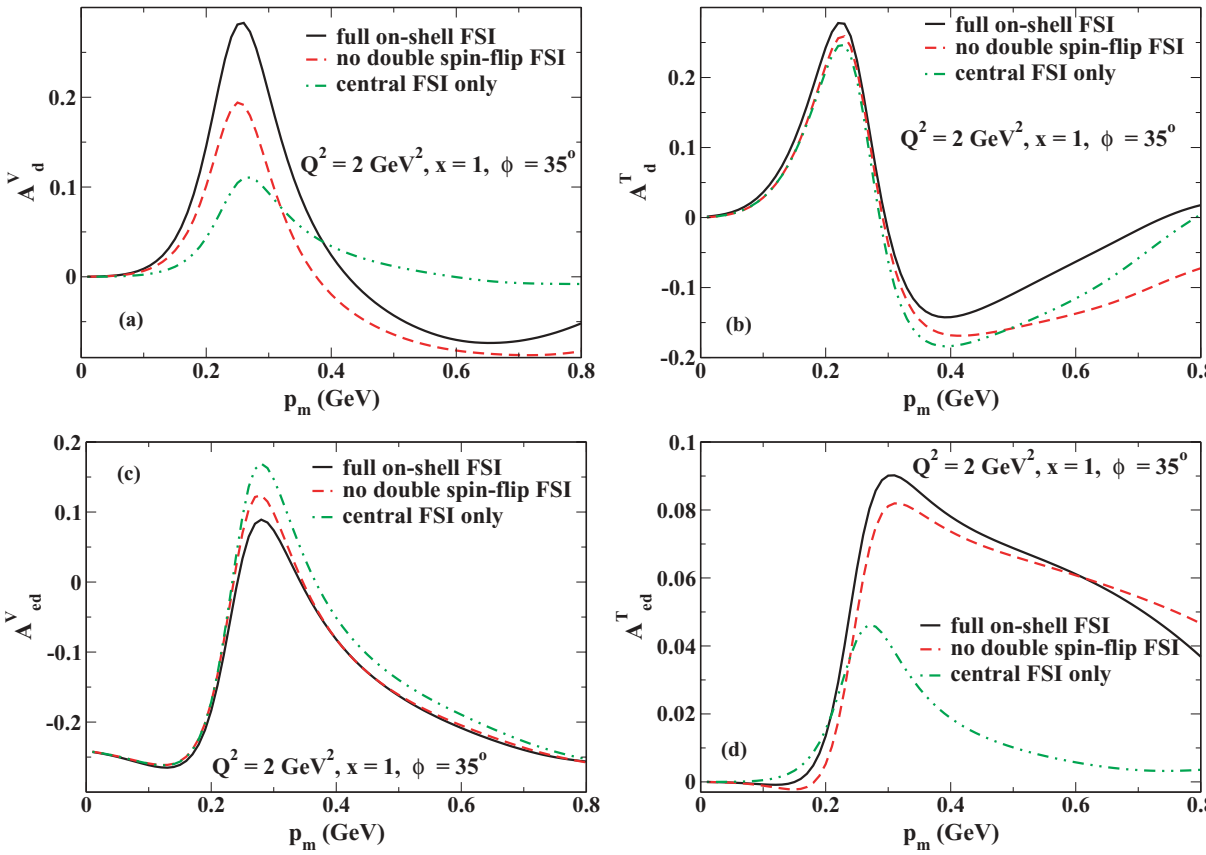

FIG. 8. (Color online) Asymmetries A_d^V (a), A_d^T (b), $A_{\rm ed}^V$ (c), and $A_{\rm ed}^T$ (d) for a beam energy of 5.5 GeV, $Q^2 = 2$ GeV^2, $x = 1$, and $\phi_p = 35^\circ$ are shown calculated with the full on-shell FSI (solid line), without any double spin-flip terms in the on-shell FSI (dashed line), and with central on-shell FSI only (dash-double-dotted line) as a function of the missing momentum.

above the full result, while the no double spin-flip result is below it. For this asymmetry, for $p_m > 0.1$ GeV, all types of spin-dependent FSI are very important. The tensor-beam asymmetry, $A_{\rm ed}^T$, shows that while the double spin-flip terms have only a small effect, the single spin-flip term, i.e., the spin-orbit term, gives a huge contribution.

Overall, the tensor asymmetry A_d^T and the double spin asymmetry $A_{\rm ed}^V$ exhibit rather similar behavior, showing some quantitative and no large qualitative dependence on spin-dependent FSIs. The target-spin asymmetry A_d^V and the tensor-beam asymmetry $A_{\rm ed}^T$ show large qualitative and quantitative sensitivity to spin-dependent FSIs, each in a different way.

In a previous paper [7] dealing with unpolarized observables, we investigated the influence of the different invariant amplitudes of the NN amplitude parametrization by calculating the FSIs with only one of the invariant amplitudes. For the unpolarized case, we found that the role of interference is huge, and that there is no single dominant amplitude. For the asymmetries, we find that for small angles, the pseudoscalar amplitude seems to be very close to all asymmetries except for $A_{\rm ed}^T$, but this behavior is confined to $\theta < 30^\circ$. Deviations beyond that are significant, in particular for A_d^V. The results show that overall, there are many relevant interference effects, and no single part of the NN amplitude is dominant.

4. *Influence of the D wave*

A question often discussed is the influence of correlations in the nuclear ground state and, in the case of the deuteron, the role played by D-wave and P-wave admixtures. Due to the rather different predictions of various nonrelativistic NN models for the D-wave content, the hunt for observables sensitive to this part of the wave function has been going on for a long time. It should be noted that on theoretical grounds, the attempts to extract the D-wave contribution to the deuteron bound state are ill considered. The wave function is not an observable, and unitary transformations can change the D-state contribution while leaving the matrix elements unchanged. Thus an actual observable contains information about initial and final states, as well as about the current operator, with the various quantities changing with unitary transformation, and one cannot be uniquely separated from the others.

In our calculation, because of the normalization of the ground-state wave function, there are some issues with directly isolating the D-wave contribution. Just to give an impression of the influence of the D-wave contribution on the asymmetries we study here, we have simply switched off the D-wave contributions, without changing the normalizations. In our relativistic calculation, there is also a P-wave contribution present. We study its effect, too. In general, P-wave effects are expected to be very small.

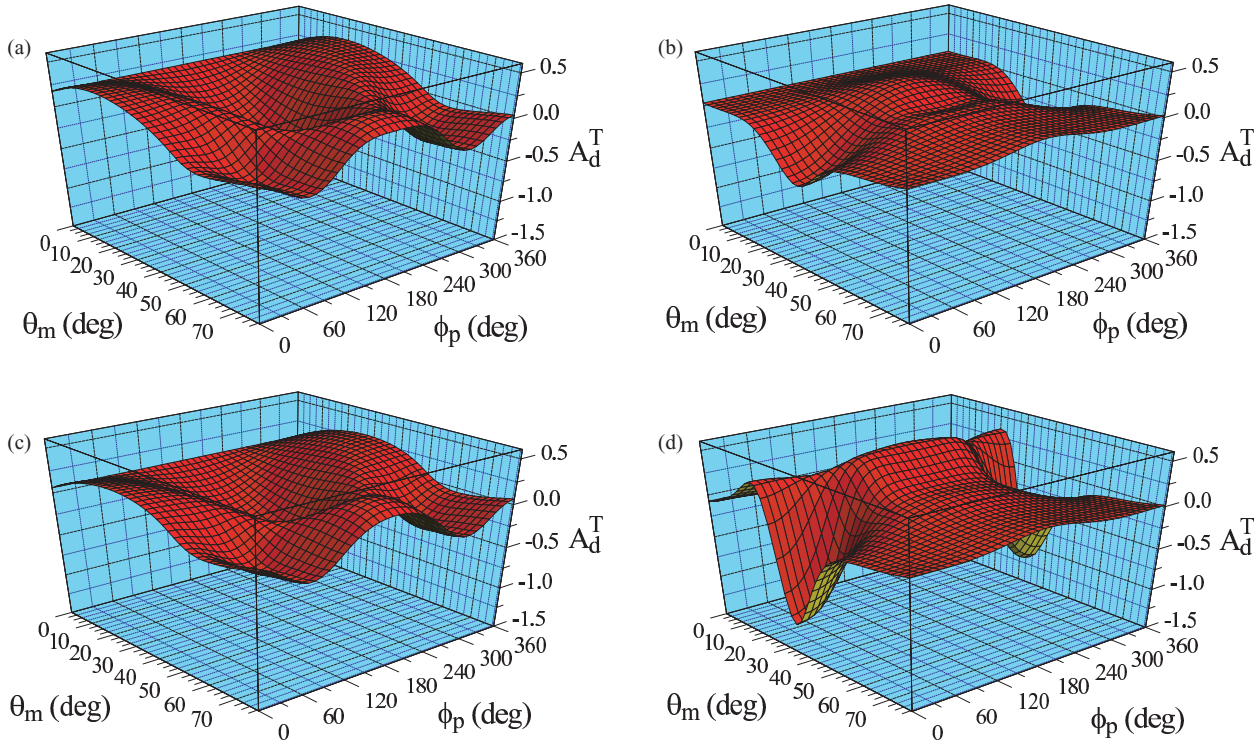

FIG. 9. (Color online) Asymmetry A_d^T, for a beam energy of 5.5 GeV, $Q^2 = 2$ GeV^2, and $p_m = 0.4$ GeV is shown calculated (a) with on-shell FSI, (b) without a D-wave contribution to the ground state, (c) without a P-wave contribution to the ground state, and (d) with only an S-wave contribution to the ground state, as a function of the polar angle of the missing momentum θ_m and the proton's azimuthal angle.

While the other asymmetries also show significant dependence on the D-wave, we will focus here for brevity on the effects of the D-wave and P-wave contributions on the tensor asymmetry A_d^T (see Fig. 9). As expected, the difference between the calculation with the full ground-state wave function [Fig. 9(a)] and the calculation without the D wave [Fig. 9(b)] is large: a prominent dip is turned into a peak, and the maximum values reached change. In nonrelativistic PWIA, this asymmetry would be zero without the D wave, but with FSI (even just central FSI), the tensor asymmetry acquires a nonzero value, because the relative positions of the neutron and the knocked-out proton influence the strength of the FSI that is experienced.

Performing a calculation without the P-wave contribution [Fig. 9(c)] does not lead to any significant changes, the peak heights vary a little, but there are no qualitative changes. Figure 9(d) shows the results for just the S-wave part of the wave function. Here, the missing P-wave contribution—still present in the top right panel without the D wave—leads to a somewhat different shape and an increased magnitude for the dip structure at lower ϕ_p values. It is interesting to note that in PWIA, if we switch off the D-wave contribution, the tensor asymmetry is small but still nonzero because of the P-wave contributions.

IV. SUMMARY AND OUTLOOK

In this paper, we have presented a formalism for the calculation of responses and asymmetries for polarized deuteron targets. We have shown how to evaluate these observables in different reference frames and for different polarization axes. Symmetries of the current matrix elements were pointed out, and together with the behavior under parity and time reversal transformations, exploited to show that two of the asymmetries we discuss, the target-spin asymmetry A_d^V and the tensor-beam asymmetry $A_{\rm ed}^T$, vanish in PWIA.

We performed a relativistic calculation of various asymmetries accessible with a polarized deuteron target. We have included a full FSI calculation, with on-shell and off-shell contributions, using experimental data on the pn scattering amplitude as input. Final state interactions are very relevant for all asymmetries in most kinematics. Two of the asymmetries vanish in PWIA and are therefore more sensitive to FSI effects, even to the off-shell FSI contributions. An important result of our paper is that even in the region of the quasielastic ridge, $x = 1$, the influence of FSIs on the asymmetries is large, and a straightforward extraction of D-wave properties from measured data will not be possible. This is true even though the influence of the D wave on the asymmetries is large, as commonly assumed. The influence of the P waves, a purely relativistic phenomenon, is generally small, unless we consider situations where the D wave is switched off.

One interesting and conspicuous feature of the asymmetries is the fact that the target-spin asymmetry A_d^V and the tensor-beam asymmetry $A_{\rm ed}^T$ have very similar properties, i.e., they vanish in PWIA, have similar sensitivity to FSIs, and a similar dependence on ϕ_p, just as the tensor asymmetry A_d^T and the beam-vector asymmetry $A_{\rm ed}^V$ show similar properties in these

respects. We have shown that this can be understood in terms of their behavior under parity and time reversal in PWIA.

We have tested the sensitivity of our results to the different parts of the FSIs. As expected, spin-dependent FSIs are relevant, and depending on the kinematics and observable, even the double spin-flip terms are extremely important.

Our calculation has been performed in an impulse approximation, i.e., assuming that the detected proton is the nucleon that interacted with the photon initially. Contributions from the Born term, where the photon interacts with the neutron, will in general be small for most observables in most kinematics, but they may contribute noticeably for larger missing momenta ($p_m > 0.6$ GeV).

It is always an interesting question to consider which observable should be measured in which kinematic region. With polarized targets and beams, experiments require a lot of effort and beam time, so very careful planning is necessary. In this paper, we have focused on the final state interaction effects, which can safely be assumed to be the major contributors to the reaction mechanism. Other mechanisms, such as meson exchange currents and isobar contributions, will be less important but might also be interesting to investigate, and they may change the FSI-only picture somewhat. Clearly, an important message from our paper is that two asymmetries each show similar behavior, so measuring one from each category will give the optimum information. If one is interested in studying FSIs, the kinematic regions with large FSI effects—both on-shell and off-shell—are attractive candidates. A measurement of the momentum distribution of A_d^V or $A_{\rm ed}^T$ at larger x, e.g., $x = 1.3$ as shown in Fig. 3, would be highly interesting. In addition, any measurement of polarized observables in regions where the unpolarized observables have already been measured might be very helpful in improving our knowledge of the reaction mechanism and the deuteron itself.

Next, we plan to perform calculations for an unpolarized deuteron target and a polarized ejected nucleon.

ACKNOWLEDGMENTS

We thank Sebastian Kuhn for his insightful comments on an earlier version of this paper. We thank Michael Kohl for providing us with information on the Bates experiments. This work was supported in part by funds provided by the US Department of Energy through a cooperative research agreement under Contract No. DE-AC05-84ER40150 and by the National Science Foundation under Grant No. PHY-0653312.

APPENDIX: THE DENSITY MATRIX

Consider an object with total angular momentum j and projection m. An arbitrary state of angular momentum j can be written as

$$|j\rangle_i = \sum_{m=-j}^{j} c_m^i |jm\rangle, \tag{A1}$$

where normalization of the state requires that

$$\sum_{m=-j}^{j} |c_m^i|^2 = 1. \tag{A2}$$

The expectation value of some operator $\hat{A}$ for this state is given by

$$\begin{aligned}\langle\hat{A}\rangle_i &= \sum_{m'=j}^{j} c_{m'}^{i\,*} \langle jm'|\hat{A} \sum_{m=-j}^{j} |jm\rangle c_m^i \\ &= \sum_{m'=j}^{j} \sum_{m=-j}^{j} \langle j, m'|\hat{A}|jm\rangle c_m^i c_{m'}^{i\,*}.\end{aligned} \tag{A3}$$

Any attempt to polarize a target consisting of a collection of these objects by applying magnetic fields will in general produce not a single state, such as that described above, but rather a statistical ensemble of such states with probabilities P_i such that

$$\sum_i P_i = 1. \tag{A4}$$

The statistical average of the expectation value of operator $\hat{A}$ is then given by

$$\langle\hat{A}\rangle = \sum_i P_i \langle\hat{A}\rangle_i = \sum_{m'=-j}^{j} \sum_{m=-j}^{j} \langle j, m'|\hat{A}|jm\rangle \sum_i c_m^i P_i c_{m'}^{i\,*}. \tag{A5}$$

Defining the density matrix

$$\rho_{mm'} = \sum_i c_m^i P_i c_{m'}^{i\,*}, \tag{A6}$$

and

$$A_{m'm} = \langle j, m'|\hat{A}|jm\rangle, \tag{A7}$$

the average expectation value of $\hat{A}$ can be written as

$$\langle\hat{A}\rangle = \sum_{m'=-j}^{j} \sum_{m=-j}^{j} A_{m'm}\rho_{mm'} = \mathrm{Tr}(\boldsymbol{A}\boldsymbol{\rho}), \tag{A8}$$

where $\boldsymbol{A}$ and $\boldsymbol{\rho}$ are the matrix representation of $\hat{A}$ and the density matrix in the subspace of total angular momentum j.

From Eq. (A6),

$$\rho_{mm'}^* = \sum_i c_{m'}^i P_i c_m^{i\,*} = \rho_{m'm}, \tag{A9}$$

or in matrix form

$$\boldsymbol{\rho}^\dagger = \boldsymbol{\rho}. \tag{A10}$$

So the density matrix is Hermitian. Also,

$$\mathrm{Tr}(\boldsymbol{\rho}) = \sum_{m=-j}^{j} \sum_i c_m^i P_i c_m^{i\,*} = \sum_i \sum_{m=-j}^{j} |c_m^i|^2 P_i = \sum_i P_i = 1. \tag{A11}$$

A further constraint on density matrix is given by

$$\mathrm{Tr}(\boldsymbol{\rho}^2) \leqslant (\mathrm{Tr}(\boldsymbol{\rho}))^2 = 1. \tag{A12}$$

It is often convenient to express the density matrix for angular momentum j in terms of spherical tensor operators such that

$$\hat{\rho} = \frac{1}{2j+1} \sum_{J=0}^{2j} \sum_{M=-J}^{J} T^*_{JM} \hat{\tau}_{JM}, \tag{A13}$$

where $\hat{\tau}_{JM}$ is an irreducible spherical tensor operator of rank J and projection M, and T_{JM} are complex coefficients that describe the average polarization of the target. These are defined such that

$$T^*_{JM} = (-1)^M T_{J-M}, \tag{A14}$$

and

$$\hat{\tau}^\dagger_{JM} = (-1)^M \hat{\tau}_{J-M}. \tag{A15}$$

Since we are concerned with a polarized deuteron target in this paper, we will now confine the argument to the case $j = 1$. In this case, matrix elements of the density operator are given by

$$\rho_{\lambda\lambda'} = \langle 1\lambda|\hat{\rho}|1\lambda'\rangle = \frac{1}{3} \sum_{J=0}^{2} \sum_{M=-J}^{J} T^*_{JM} \langle 1\lambda|\hat{\tau}_{JM}|1\lambda'\rangle. \tag{A16}$$

This can be written in matrix form as

$$\boldsymbol{\rho} = \frac{1}{3} \sum_{J=0}^{2} \sum_{M=-J}^{J} T^*_{JM} \boldsymbol{\tau}_{JM}. \tag{A17}$$

If we choose normalizations such that

$$T_{00} = 1, \tag{A18}$$

and

$$\langle 1||\hat{\tau}_J||1\rangle = \sqrt{3}\sqrt{2J+1}, \tag{A19}$$

the matrices $\boldsymbol{\tau}_{JM}$ are

$$\boldsymbol{\tau}_{00} = \begin{pmatrix} 1 & 0 & 0 \\ 0 & 1 & 0 \\ 0 & 0 & 1 \end{pmatrix},$$

$$\boldsymbol{\tau}_{10} = \sqrt{\frac{3}{2}} \begin{pmatrix} 1 & 0 & 0 \\ 0 & 0 & 0 \\ 0 & 0 & -1 \end{pmatrix}, \qquad \boldsymbol{\tau}_{11} = \sqrt{\frac{3}{2}} \begin{pmatrix} 0 & -1 & 0 \\ 0 & 0 & -1 \\ 0 & 0 & 0 \end{pmatrix},$$

$$\boldsymbol{\tau}_{20} = \frac{1}{\sqrt{2}} \begin{pmatrix} 1 & 0 & 0 \\ 0 & -2 & 0 \\ 0 & 0 & 1 \end{pmatrix}, \qquad \boldsymbol{\tau}_{21} = \sqrt{\frac{3}{2}} \begin{pmatrix} 0 & -1 & 0 \\ 0 & 0 & 1 \\ 0 & 0 & 0 \end{pmatrix},$$

$$\boldsymbol{\tau}_{22} = \sqrt{3} \begin{pmatrix} 0 & 0 & 1 \\ 0 & 0 & 0 \\ 0 & 0 & 0 \end{pmatrix}, \tag{A20}$$

and the remaining matrices can be obtained from

$$\boldsymbol{\tau}^\dagger_{JM} = (-1)^M \boldsymbol{\tau}_{J-M}. \tag{A21}$$

These matrices have the properties

$$\mathrm{Tr}(\boldsymbol{\tau}_{JM}) = 0, \tag{A22}$$

and

$$\mathrm{Tr}(\boldsymbol{\tau}^\dagger_{J'M'} \boldsymbol{\tau}_{JM}) = 3\delta_{J'J}\delta_{M'M}. \tag{A23}$$

So,

$$\mathrm{Tr}(\boldsymbol{\tau}^\dagger_{JM} \boldsymbol{\rho}) = T^*_{JM}. \tag{A24}$$

The constraint given in Eq. (A12) requires that

$$\frac{1}{3}\left(1 + \sum_{J=1}^{2} \sum_{M=-J}^{J} |T_{JM}|^2\right) \leqslant 1. \tag{A25}$$

Using the matrices defined by Eq. (A20), we can write

$$\boldsymbol{\rho}^D = \frac{1}{3}\left\{\mathbf{1} + \sum_{J=1}^{2}\left[T_{J0}\boldsymbol{\tau}_{J0} + \sum_{M=1}^{J}(T^*_{JM}\boldsymbol{\tau}_{JM} + T^*_{J-M}\boldsymbol{\tau}_{J-M})\right]\right\}. \tag{A26}$$

The last term of this can be rewritten using Eq. (A14) to give

$$\begin{aligned} &\sum_{M=1}^{J}(T^*_{JM}\boldsymbol{\tau}_{JM} + T^*_{J-M}\boldsymbol{\tau}_{J-M}) \\ &\quad = \sum_{M=1}^{J}(T^*_{JM}\boldsymbol{\tau}_{JM} + (-1)^M T_{JM}\boldsymbol{\tau}_{J-M}) \\ &\quad = \sum_{M=1}^{J}[\mathrm{Re}(T_{JM})(\boldsymbol{\tau}_{JM} + (-1)^M\boldsymbol{\tau}_{J-M}) \\ &\qquad + \mathrm{Im}(T_{JM})(-i)(\boldsymbol{\tau}_{JM} - (-1)^M\boldsymbol{\tau}_{J-M})] \\ &\quad = \sum_{M=1}^{J}\left(\mathrm{Re}(T_{JM})\boldsymbol{\tau}^{\mathrm{Re}}_{JM} + \mathrm{Im}(T_{JM})\boldsymbol{\tau}^{\mathrm{Im}}_{JM}\right), \end{aligned} \tag{A27}$$

where

$$\boldsymbol{\tau}^{\mathrm{Re}}_{JM} = \boldsymbol{\tau}_{JM} + (-1)^M\boldsymbol{\tau}_{J-M} = \boldsymbol{\tau}_{JM} + \boldsymbol{\tau}^\dagger_{JM}, \tag{A28}$$

and

$$\boldsymbol{\tau}^{\mathrm{Im}}_{JM} = -i(\boldsymbol{\tau}_{JM} - (-1)^M\boldsymbol{\tau}_{J-M}) = -i(\boldsymbol{\tau}_{JM} - \boldsymbol{\tau}^\dagger_{JM}). \tag{A29}$$

The orthogonality relations for the $\boldsymbol{\tau}_{JM}$ can be used to show that

$$\mathrm{Tr}\left[\boldsymbol{\tau}^{\mathrm{Re}\,\dagger}_{JM}\boldsymbol{\rho}^D\right] = 2\mathrm{Re}(T_{JM}), \tag{A30}$$

and

$$\mathrm{Tr}\left[\boldsymbol{\tau}^{\mathrm{Im}\,\dagger}_{JM}\boldsymbol{\rho}^D\right] = 2\mathrm{Im}(T_{JM}). \tag{A31}$$

[1] J. Ryckebusch, W. Cosyn, B. Van Overmeire, and C. Martinez, Eur. Phys. J. A **31**, 585 (2007); J. Ryckebusch, P. Lava, M. C. Martinez, J. M. Udias, and J. A. Caballero, Nucl. Phys. **A755**, 511 (2005); P. Lava, M. C. Martinez, J. Ryckebusch, J. A. Caballero, and J. M. Udias, Phys. Lett. **B595**, 177 (2004); L. L. Frankfurt, W. R. Greenberg, G. A. Miller, M. M. Sargsian, and M. I. Strikman, Z. Phys. A **352**, 97 (1995).

[2] J. Lachniet *et al.* (CLAS Collaboration), Phys. Rev. Lett. **102**, 192001 (2009).

[3] L. Frankfurt, M. Sargsian, and M. Strikman, Int. J. Mod. Phys. A **23**, 2991 (2008).

[4] M. Garcon and J. W. Van Orden, Adv. Nucl. Phys. **26**, 293 (2001).

[5] R. A. Gilman and F. Gross, J. Phys. G **28**, R37 (2002).

[6] I. Sick, Prog. Part. Nucl. Phys. **47**, 245 (2001).
[7] S. Jeschonnek and J. W. Van Orden, Phys. Rev. C **78**, 014007 (2008).
[8] F. Gross, J. W. Van Orden, and K. Holinde, Phys. Rev. C **41**, R1909 (1990); **45**, 2094 (1992).
[9] R. A. Arndt, W. J. Briscoe, I. I. Strakovsky, and R. L. Workman, Phys. Rev. C **76**, 025209 (2007). Data available through SAID, http://gwdac.phys.gwu.edu/.
[10] M. M. Sargsian, Int. J. Mod. Phys. E **10**, 405 (2001); M. M. Sargsian, T. V. Abrahamyan, M. I. Strikman, and L. L. Frankfurt, Phys. Rev. C **71**, 044614 (2005); L. L. Frankfurt, M. M. Sargsian, and M. I. Strikman, *ibid.* **56**, 1124 (1997).
[11] J. Ryckebusch, D. Debruyne, P. Lava, S. Janssen, B. Van Overmeire, and T. Van Cauteren, Nucl. Phys. **A728**, 226 (2003); D. Debruyne, J. Ryckebusch, W. Van Nespen, and S. Janssen, Phys. Rev. C **62**, 024611 (2000); B. Van Overmeire and J. Ryckebusch, Phys. Lett. **B650**, 337 (2007); W. Cosyn and J. Ryckebusch, Phys. Rev. C **80**, 011602 (2009).
[12] C. Ciofi degli Atti and L. P. Kaptari, Phys. Rev. C **71**, 024005 (2005); Phys. Rev. Lett. **100**, 122301 (2008); C. Ciofi degli Atti, L. P. Kaptari, and D. Treleani, Phys. Rev. C **63**, 044601 (2001).
[13] J. M. Laget, Phys. Lett. **B609**, 49 (2005).
[14] R. Schiavilla, O. Benhar, A. Kievsky, L. E. Marcucci, and M. Viviani, Phys. Rev. C **72**, 064003 (2005).
[15] W. Boeglin, M. Jones, A. Klein, P. Ulmer, J. Mitchell, and E. Voutier, spokespersons, Jefferson Lab Experiment E01–020.
[16] K. S. Egiyan *et al.* (CLAS Collaboration), Phys. Rev. Lett. **96**, 082501 (2006); Phys. Rev. C **68**, 014313 (2003).
[17] A. Maschinot, Ph.D. thesis, MIT, 2005, BLAST data from MIT Bates.
[18] G. Gilfoyle, spokesperson, Jefferson Lab Hall B, E5 run period; G. P. Gilfoyle (CLAS Collaboration), Bull. Am. Phys. Soc., Fall DNP Meeting, DF.00010, 2006.
[19] W. Boeglin, spokesperson, proposal to Jefferson Lab PAC 33, 2007.
[20] G. Dodge, S. Kuhn, and M. Taiuti, spokespersons, Jefferson Lab 93-009 (EG1 run group).
[21] I. Passchier *et al.*, Phys. Rev. Lett. **88**, 102302 (2002).
[22] E. Geis *et al.* (BLAST Collaboration), Phys. Rev. Lett. **101**, 042501 (2008).
[23] H. Arenhövel, W. Leidemann, and E. L. Tomusiak, Z. Phys. A **331**, 123 (1988); Phys. Rev. C **46**, 455 (1992).
[24] A. Bianconi, S. Jeschonnek, N. N. Nikolaev, and B. G. Zakharov, Phys. Rev. C **53**, 576 (1996).
[25] A. S. Raskin and T. W. Donnelly, Ann. Phys. (NY) **191**, 78 (1989).
[26] V. Dmitrasinovic and F. Gross, Phys. Rev. C **40**, 2479 (1989).
[27] F. Gross, Phys. Rev. **186**, 1448 (1969); Phys. Rev. D **10**, 223 (1974); Phys. Rev. C **26**, 2203 (1982).